



Article

Fenton Reaction for Enhancing Polishing Rate and Protonated Amine Functional Group Polymer for Inhibiting Corrosion in Ge₁Sb₄Te₅ Film Surface Chemical-Mechanical-Planarization

Gi-Ppeum Jeong ¹, Young-Hye Son ², Jun-Seong Park ¹, Pil-Su Kim ², Man-Hyup Han ², Seong-Wan Hong ², Jin-Hyung Park ³ , Hao Cui ⁴, Bo-Un Yoon ⁴ and Jea-Gun Park ^{1,2,*} 

¹ Department of Electronic Engineering, Hanyang University, Seoul 04763, Korea; bono23231@naver.com (G.-P.J.); silversmith_@naver.com (J.-S.P.)

² Department of Nanoscale Semiconductor Engineering, Hanyang University, Seoul 04763, Korea; younghyeee90@naver.com (Y.-H.S.); psk6208@naver.com (P.-S.K.); aksguq06@naver.com (M.-H.H.); mouse2058@naver.com (S.-W.H.)

³ UB Materials Inc., Yongin 17162, Korea; parkjinhyung@gmail.com

⁴ Flash Process Development Team, Semiconductor R&D Center, Samsung Electronics, Samsungjeonja-ro, Hwaseong 18448, Korea; hao14.cui@samsung.com (H.C.); B.yoon@samsung.com (B.-U.Y.)

* Correspondence: parkjgl@hanyang.ac.kr



Citation: Jeong, G.-P.; Son, Y.-H.; Park, J.-S.; Kim, P.-S.; Han, M.-H.; Hong, S.-W.; Park, J.-H.; Cui, H.; Yoon, B.-U.; Park, J.-G. Fenton Reaction for Enhancing Polishing Rate and Protonated Amine Functional Group Polymer for Inhibiting Corrosion in Ge₁Sb₄Te₅ Film Surface Chemical-Mechanical-Planarization. *Appl. Sci.* **2021**, *11*, 10872. <https://doi.org/10.3390/app112210872>

Academic Editors: Jihoon Seo and Kangchun Lee

Received: 28 October 2021

Accepted: 16 November 2021

Published: 17 November 2021

Publisher's Note: MDPI stays neutral with regard to jurisdictional claims in published maps and institutional affiliations.



Copyright: © 2021 by the authors. Licensee MDPI, Basel, Switzerland. This article is an open access article distributed under the terms and conditions of the Creative Commons Attribution (CC BY) license (<https://creativecommons.org/licenses/by/4.0/>).

Abstract: A Fenton reaction and a corrosion inhibition strategy were designed for enhancing the polishing rate and achieving a corrosion-free Ge₁Sb₄Te₅ film surface during chemical-mechanical planarization (CMP) of three-dimensional (3D) cross-point phase-change random-access memory (PCRAM) cells and 3D cross-point synaptic arrays. The Fenton reaction was conducted with 1,3-propylenediamine tetraacetic acid, ferric ammonium salt (PDTA-Fe) and H₂O₂. The chemical oxidation degree of GeO₂, Sb₂O₃, and TeO₂ evidently increased with the PDTA-Fe concentration in the CMP slurry, such that the polishing rate of the Ge₁Sb₄Te₅ film surface linearly increased with the PDTA-Fe concentration. The addition of a corrosion inhibitor having protonated amine functional groups in the CMP slurry remarkably suppressed the corrosion degree of the Ge₁Sb₄Te₅ film surface after CMP; i.e., the corrosion current of the Ge₁Sb₄Te₅ film surface linearly decreased as the corrosion inhibitor concentration increased. Thus, the proposed Fenton reaction and corrosion inhibitor in the Ge₁Sb₄Te₅ film surface CMP slurry could achieve an almost recess-free Ge₁Sb₄Te₅ film surface of the confined-PCRAM cells, having an aspect ratio of 60-nm-height to 4-nm-diameter after CMP.

Keywords: chemical-mechanical planarization; phase-change random-access memory; Fenton reaction; ferric-ionic catalyst; corrosion inhibitor; chalcogenide

1. Introduction

Recently, memory semiconductor device technologies have evolved to achieve fast switching, low-power consumption, and low memory bit-cost via the scaling-down of memory cells. Thus, two types of memory devices have been classified in terms of switching speed, power consumption, and cost per bit: dynamic random-access memory (DRAM) and three-dimensional (3D) NAND flash memory [1–3]. However, a 3D cross-point memory using phase-change random-access memory (PCRAM) has been proposed to generate a new storage memory in the memory hierarchy. Unlike DRAM, 3D cross-point PCRAM-based memory has demonstrated a nonvolatile memory characteristic with a fast operation speed of several hundred nanoseconds, and an excellent write-and-erase endurance cycle of $>1 \times 10^8$ [4–17]. In addition, a cross-point synaptic array using PCRAM has been extensively researched for neuromorphic hardware performing parallel computing, because PCRAM can supply a large resistance ratio to achieve a sufficient synaptic weight range, low-power consumption due to fast switching, and good scalability for synaptic array [18–21]. In general, 3D cross-point PCRAM cells have been fabricated, and PCRAM-cells have a

confined memory cell structure and a chalcogenide-based nonlinear-selector vertically stacked on the confined memory cell. Note that a confined memory cell structure with a vertical structure of the top electrode, PCRAM material filled in a confined hole, and bottom electrode are essential for minimizing the reset current. In addition, a chalcogenide-based nonlinear-selector stacked vertically on the confined memory cell is necessary for suppressing an integrated leakage current in a memory cell array.

To fabricate a confined PCRAM-cell structure, a PCRAM material such as $\text{Ge}_x\text{Sb}_y\text{Te}_z$ or Ge or N₂ doped Sb_yTe_z , etc., called a GST film, should be filled in the confined hole structure with a high aspect ratio of >10 [22]. Thus, sputtering followed by annealing, chemical vapor deposition (CVD), or atomic layer deposition (ALD) of a GST film in a confined-hole structure is utilized. Then, chemical-mechanical planarization (CMP) should be performed to eliminate the over-burdening of the GST film deposited on the confined hole structure and should be stopped as soon as a CMP stopping layer (i.e., Si_3N_4 film surface) is exposed during the CMP process. It should be noted that CMP is conducted by a chemical reaction between the CMP slurry and the GST film surface as well as rubbing between nanoscale abrasives in the CMP slurry and the GST film surface. In particular, the GST films produced by CVD or ALD present a high chemical reactivity and extremely low mechanical hardness, so that the CMP of the GST film surface can easily result in corrosion of the GST film surface or surface-tensile-stress induced polishing-void after CMP. To avoid corrosion or polishing-void, the addition of an oxidizer (i.e., H_2O_2) in the GST film surface CMP slurry is essential, which can passivate the GST film surface by forming a chemical oxidizer layer on the GST film surface. However, an oxidizer significantly reduces the polishing-rate of the GST film surface and cannot completely prevent the generation of a corrosion or polishing-induced-void on the GST film surface after a CMP [22,23]. In addition, the research has been reported for enhancing the GST film surface polishing-rate, presenting that the pH design of the GST film surface CMP slurry would be a key parameter to determine the GST-film surface polishing-rate [24,25].

In our study, to simultaneously enhance the polishing rate of the GST film surface and suppress surface corrosion during CMP, a novel GST film surface CMP slurry was designed with the introduction of the Fenton reaction and the addition of a columbic-interactive corrosion inhibitor. In general, the Fenton reaction has been used to accelerate the chemical oxidation degree of W or Cu during a CM via chemical decomposition of H_2O_2 into dissolved O_2 and radicals [26–28]. However, for the first time, the Fenton reaction in the CMP slurry was introduced for the GST film surface CMP by designing a proper ferric-ionic catalyst working at a strong acid pH. Consequently, six different types of catalysts were evaluated: ferric-sulfate (i.e., Fe-sulfate), ferric oxalate (i.e., Fe-oxalate), ferric-nitride (i.e., Fe-nitride), PDTA-Fe, ferric-citrate (i.e., Fe-citrate), and ferric cyanide (i.e., Fe-cyanide) as shown in Table S1. Among them, PDTA-Fe as a ferric-ionic catalyst was selected, and the dependencies of GST- and Si_3N_4 film surface polishing rate on the PDTA-Fe concentration in the CMP slurry were estimated. In addition, the dependencies of the static corrosion etch rate and surface roughness on the PDTA-Fe concentration were investigated, and their mechanism characterized by observing the chemical composition of the GST film surface depending on the PDTA-Fe concentration of the CMP slurry. Moreover, the effect of a corrosion inhibitor (i.e., polyethylenimine (PEI)) on the corrosion current reduction of the GST film surface and its mechanism was delineated by investigating the chemical composition of the GST film surface depending on the PEI concentration in the slurry. Note that polyethylenimine (i.e., PEI) is a polymer corrosion inhibitor having protonated amine functional group and can produce a nanoscale-thick polymer-passivation-layer on the GST film surface, so that the presence of corrosion on the GST film surface can be avoided. Finally, the dependencies of the GST- and Si_3N_4 film surface polishing rate on the PEI concentration in the CMP slurry and the dependency of the polishing-induced recess on the PEI concentration in the slurry was estimated.

2. Materials and Methods

2.1. Materials

For a blanket Ge₁Sb₄Te₅ film wafer, a 70-nm-thick Ge₁Sb₄Te₅ film was deposited on a 12-inch-diameter Si wafer by physical vapor deposition. This was followed by laser annealing for several nanoseconds. In addition, for a PRAM-cell-array patterned wafer, a 30-nm-thick Si₃N₄ film was deposited as a stopping layer. Then, the confined-holes having a 4-nm diameter and a 60.7-nm height was produced by lithography and etching of a SiO₂ insulating layer deposited on the stopping layer. Finally, ~30-nm-thick Ge₁Sb₄Te₅ film was deposited on confined-holes. The Ge₁Sb₄Te₅ film surface CMP slurries were produced using 70-nm colloidal silica abrasives (i.e., Fuso PL-7 solution), an oxidant H₂O₂ (Junsei Chemical Co., Ltd., Tokyo, Japan), a pH titrant (i.e., HNO₃), a Fenton reaction catalyst (i.e., 1,3-Propylenediamine tetraacetic acid, ferric ammonium salt: PDTA–Fe, Chelest Co., Ltd., Osaka, Japan), and corrosion inhibitor (i.e., polyethylenimine: PEI with a molecular weight of 25,000 g/mol, Sigma Aldrich, Saint Louis, MO, USA). The slurries used in our experiment were composed of 1-wt% 70-nm colloidal silica abrasives, 1-wt% oxidant H₂O₂, 0.01~0.05-wt% PDTA–Fe, and 0~0.09-wt% PEI, which was titrated at pH 2 using HNO₃. For slurry stability, sonication treatment for all the slurries was conducted.

2.2. Chemical-Mechanical Planarization

The blanket or patterned Ge₁Sb₄Te₅-film deposited 12-inch-wafers were cut into 4 × 4 cm squares. The CMP of the blanket or patterned Ge₁Sb₄Te₅-film surface was conducted using a CMP polisher (POLI-300, G&P Tech. Inc., Pusan, Korea) attached to an industry standard CMP pad (IC 1000/Suba IV, Dow Chemical, Michigan, MI, USA). A pad break-in for warm polishing was carried out with a diamond conditioner for 10 min, and then two SiO₂ film dummy wafers were polished prior to the main polishing of the blanket or patterned Ge₁Sb₄Te₅ film surface. In situ pad conditioning was conducted after each polishing for various slurries. The applied head pressure was 6 psi, the rotation speed of the carrier holding the blanket or patterned Ge₁Sb₄Te₅ film samples was 70 rpm, and the rotation speed of the table attached to the CMP pad was 70 RPM/min. The flow rate of the CMP slurry was fixed at 100 mL/min, and the polishing time was set at 60 s. After 1 min of CMP, all blanket or patterned Ge₁Sb₄Te₅ film samples were buffed with DI water for 30 s to eliminate the remaining abrasives on the blanket or patterned Ge₁Sb₄Te₅ film surface.

2.3. Measurement Equipment

The polishing rate of the Ge₁Sb₄Te₅ film surface was estimated by measuring the Ge₁Sb₄Te₅ film thickness before and after CMP using ellipsometry (V-VASE, J.A. Woollam Co., Inc., Lincoln, NE, USA). Scanning electron microscopy (SEM, S-4800, Hitachi, Tokyo, Japan) image of the Ge₁Sb₄Te₅ film surface after CMP and etching was observed at an acceleration voltage of 15 kV. The surface roughness of the Ge₁Sb₄Te₅ film surface after etching was estimated by atomic force microscopy (AFM, Park system, Suwon, Korea), and the corrosion potential and current were measured using a potentiostat (CH750, CH Instruments, Austin, TX, USA). The chemical composition of the Ge₁Sb₄Te₅ film surface after etching and CMP were characterized using X-ray photoelectron spectroscopy (K-Alpha+, Thermo Fisher Scientific, Waltham, MA, USA) at 12 keV and 6 mA with a KE source of Al K α (1486.6 eV). Cross-sectional LRB-x-RRB-images of the confined memory cells before and after the CMP pattern film were observed using high-resolution transmission electron microscopy (HR-TEM, JEM-2010, JEOL, Tokyo, Japan) with an accelerating voltage of 200 kV.

3. Results and Discussion

3.1. Effect of Fenton Reaction on Enhancement in Ge₁Sb₄Te₅ Film Polishing Rate and Corrosion Suppression during CMP

As a PCRAM-cell material, an as-sputter ternary-chalcogenide film, such as Ge₁Sb₄Te₅ film, was laser-annealed at 20 mJ for 10 μ s, which was well crystallized with a face-centered

cubic structure of (200), (220), (222), and (111) dimensions, as shown in Figure S1a. The annealing did not enhance the film density (i.e., $\sim 6 \text{ g/cm}^3$) or the mean film hardness ($\sim 3 \text{ GPa}$), as shown in Figure S1b,c. In general, a CMP of chalcogenide film surface (i.e., $\text{Ge}_1\text{Sb}_4\text{Te}_5$ film) is conducted by chemical oxidation on the chalcogenide film surface, followed by mechanical rubbing between abrasives in the CMP slurry and the chalcogenide film surface. Chemical oxidation on the chalcogenide film surface, such as GeO_2 , Sb_2O_3 , and TeO_2 , requires a CMP slurry with a pH of 1–9, as shown in the Ge, Sb, and Te Pourbaix diagrams in Figure S2. To investigate the degree of chemical oxidation on the $\text{Ge}_1\text{Sb}_4\text{Te}_5$ film surface, the dependence of the chemical oxidation degree on the oxidant (i.e., H_2O_2) concentration was examined by dipping a $\text{Ge}_1\text{Sb}_4\text{Te}_5$ film at 70°C for 5 min, followed by surface chemical composition analysis by XPS. The $2p\ 3/2$ peaks of Ge and GeO_2 were found at 1217.3 and 1220.2 eV, respectively, as shown in Figure 1a. The $2p\ 3/2$ peak intensity of GeO_2 rapidly increased with a H_2O_2 concentration of 1-wt% and then slightly increased with increasing H_2O_2 concentration, while that of Ge decreased abruptly up to a H_2O_2 concentration of 1-wt% and then decreased slightly with increasing H_2O_2 concentration, as shown in the inset of Figure 1a. In addition, the $3d\ 3/2$ and $3d\ 5/2$ peak intensities of Sb were located at both 538.1 and 528.1 eV, while those of Sb_2O_3 were presented at both 539.6 and 530 eV, respectively, as shown in Figure 1b. The $3d\ 3/2$ and $3d\ 5/2$ peak intensities of Sb_2O_3 at 539.6 and 530 eV considerably increased with the H_2O_2 concentration and then saturated at a H_2O_2 concentration of 3-wt%, while the Sb peak intensities slowly decreased until there was a H_2O_2 concentration of 3-wt%, as shown in the inset of Figure 1b. The peak intensity of Sb $3d\ 5/2$ at 528.1 eV (i.e., 56,454 a.u.) was higher than that of Sb $3d\ 3/2$ at 538.1 eV (i.e., 35,261 a.u.). Furthermore, the $3d\ 3/2$ and $3d\ 5/2$ peaks of TeO_2 were discovered at 586.4 and 576 eV, while those of Te were detected at 583.4 and 573 eV, respectively, as shown in Figure 1c. Both $3d\ 3/2$ and $3d\ 5/2$ peak intensities of TeO_2 increased slightly with H_2O_2 concentration and then saturated at a H_2O_2 concentration of 2-wt%, while those of Te weakly decreased with increasing H_2O_2 concentration and then saturated at a H_2O_2 concentration of 2-wt%. Comparing Figure 1a–c, a higher XPS peak intensity was observed for Sb_2O_3 (421,875 a.u.), TeO_2 (160,629 a.u.), and GeO_2 (158,978 a.u.), indicating that the chemical oxidation degree of the $\text{Ge}_1\text{Sb}_4\text{Te}_5$ film surface was highly sequenced by Sb, Te, and Ge atoms.

Generally, a $\text{Ge}_x\text{Se}_y\text{Te}_z$ film surface CMP slurry uses an oxidizer to enhance the polishing rate, inducing corrosion pits on the $\text{Ge}_x\text{Se}_y\text{Te}_z$ film surface after CMP [22,23]. To enhance the $\text{Ge}_x\text{Se}_y\text{Te}_z$ film surface polishing rate and to avoid corrosion pits simultaneously, the Fenton reaction between the ferric-ionic catalyst and oxidizer was introduced for a $\text{Ge}_x\text{Se}_y\text{Te}_z$ film surface CMP slurry. Examining the slurry stability (i.e., no sedimentation of colloidal abrasives in a CMP slurry) among Fenton reaction catalysts such as ferric-sulfate, ferric oxalate, ferric-nitride, PDTA-Fe, ferric-citrate, and ferric cyanide, PDTA-Fe showed good slurry stability and a relatively high $\text{Ge}_1\text{Se}_4\text{Te}_5$ film surface polishing rate, as shown in Figures 2 and S3. Without the Fenton reaction in a CMP slurry (i.e., only using oxidizer H_2O_2 of 1.0-wt%), the $\text{Ge}_1\text{Se}_4\text{Te}_5$ film surface polishing-rate was $\sim 27 \text{ nm/min}$. However, the $\text{Ge}_1\text{Se}_4\text{Te}_5$ film surface polishing rate increased considerably from 27 to 105 nm/min when the PDTA-Fe concentration increased from 0 to 0.05-wt%, as shown in Figure 2, indicating that the Fenton reaction significantly enhanced the polishing rate of the $\text{Ge}_1\text{Se}_4\text{Te}_5$ film surface. In addition, the Si_3N_4 film surface polishing-rate slightly and exponentially increased from 1.3 to 6.0 nm/min , which should be reduced because the Si_3N_4 film surface should be utilized as a polishing stopping layer.

The dependency of the static corrosion rate (i.e., static etch rate) on the PDTA-Fe concentration was investigated after dipping $\text{Ge}_1\text{Se}_4\text{Te}_5$ films into slurries composed of 1.0-wt% H_2O_2 (i.e., oxidizer) of 1.0-wt%, PDTA-Fe (i.e., Fenton reaction catalyst) of 0, 0.01, 0.02, 0.03, 0.04, and 0.05-wt%, and HNO_3 (titrant) for 5 min at 70°C , as shown in Figure 3. Note that the pad temperature of the $\text{Ge}_1\text{Sb}_4\text{Te}_5$ film CMP was $\sim 70^\circ\text{C}$. As soon as PDTA-Fe 0.01-wt% was added to the slurry, the static corrosion rate rapidly decreased from 60.0 to 7.5 nm/min . Then, it slightly decreased from 8.8 to 3 nm when the PDTA-Fe concentration

increased from 0.01 to 0.05-wt%. The SEM images of the $\text{Ge}_1\text{Sb}_4\text{Te}_5$ film surface after dipping into the slurries revealed the presence of corrosion-induced pits. Many of the corrosion pits of 10–50 μm in size were found without the Fenton reaction (i.e., only using H_2O_2), as shown in the SEM image in Figure 3. The number and size of corrosion pits decreased when the PDTA–Fe concentration increased from 0 to 0.02-wt%, as shown in (i)–(iii) SEM images of Figure 3. When further increasing the PDTA–Fe concentration from 0.03 to 0.05-wt%, corrosion pits could not be found, as shown in (iv)–(vi) SEM images of Figure 3.

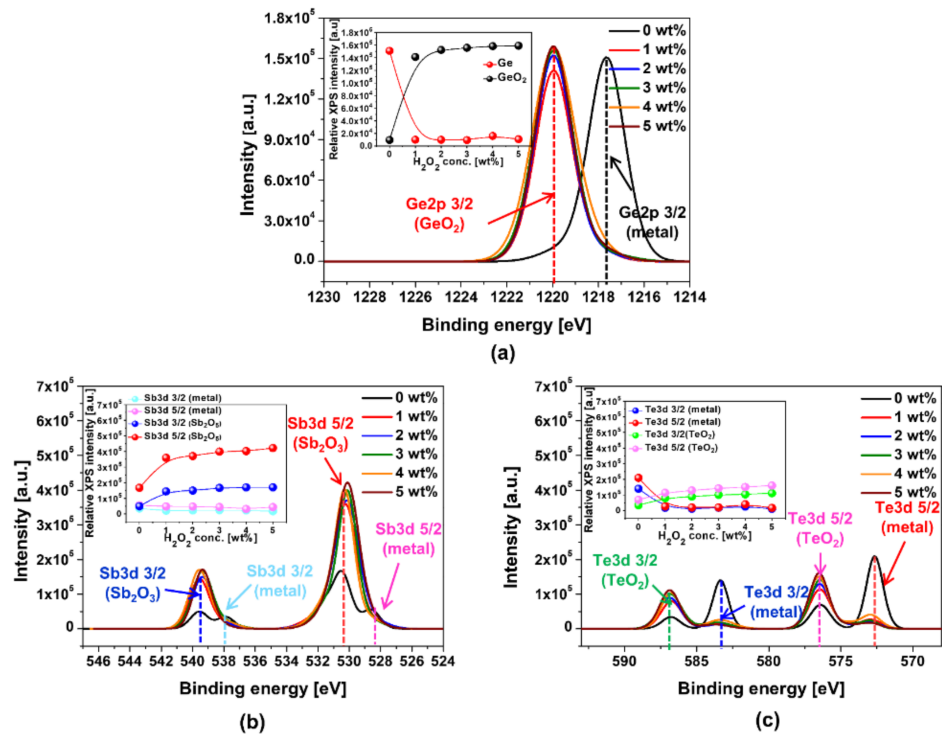


Figure 1. Dependency of chemical composition of $\text{Ge}_1\text{Sb}_4\text{Te}_5$ film surface on oxidant (i.e., H_2O_2) concentration. (a) Ge 2p spectra, (b) Sb 3d spectra, and (c) Te 3d spectra.

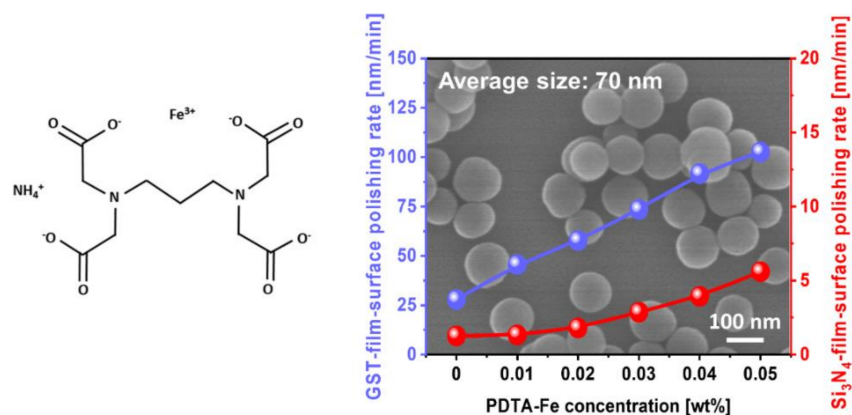


Figure 2. Dependency of $\text{Ge}_1\text{Se}_4\text{Te}_5$ - and Si_3N_4 films polishing-rate on ferric-ionic catalyst (i.e., PDTA–Fe) concentration. PDTA–Fe is decomposed of Fe^{3+} , NH_4^+ , and $[\text{C}_{11}\text{H}_{14}\text{N}_2\text{O}_8]^{4-}$ in the acid (i.e., pH 2.0) slurry. The average diameter of colloidal silica abrasives was 70 nm, as shown in inset SEM image.

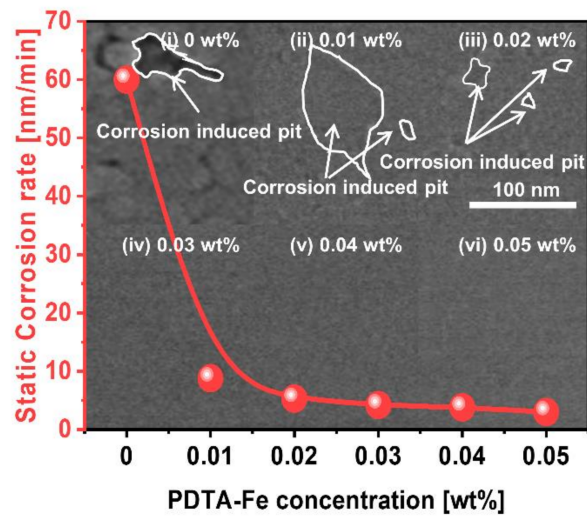


Figure 3. Dependency of static etch rate (SER) of $\text{Ge}_1\text{Sb}_4\text{Te}_5$ film surface on ferric-ionic catalyst (i.e., PDTA-Fe) concentration after dipping of $\text{Ge}_1\text{Sb}_4\text{Te}_5$ film surface into slurries. The background SEM images investigated the presence of corrosion-induced pits on the $\text{Ge}_1\text{Sb}_4\text{Te}_5$ film surface after dipping.

In addition, the AFM images, having the scanning area of $5 \mu\text{m} \times 5 \mu\text{m}$ as shown in Figure 4, of the $\text{Ge}_1\text{Sb}_4\text{Te}_5$ film surface after dipping into the slurries were observed as a function of the PDTA-Fe concentration. Without the ferric-ionic catalyst, the surface roughness magnitude (i.e., root-mean-square (Rq)) of the $\text{Ge}_1\text{Sb}_4\text{Te}_5$ film surface was ~ 3.021 nm. The Rq of the $\text{Ge}_1\text{Sb}_4\text{Te}_5$ film surface evidently decreased from 2.772 to 1.230 nm when the PDTA-Fe concentration was increased from 0.01 to 0.05-wt%. This result indicates that the introduction of the Fenton reaction in the slurry could suppress the static corrosion via chemical passivation (i.e., oxidation), in which the dissolved O_2 and radicals (i.e., HO_2^\bullet and OH^\bullet) chemically reacted with Ge, Sb, and Te atoms in the $\text{Ge}_1\text{Sb}_4\text{Te}_5$ film surface. As mentioned earlier, the dissolved O_2 and O_2^- radicals were produced by the Fenton reaction between the Fe^{3+} catalyst and H_2O_2 in the CMP slurry.

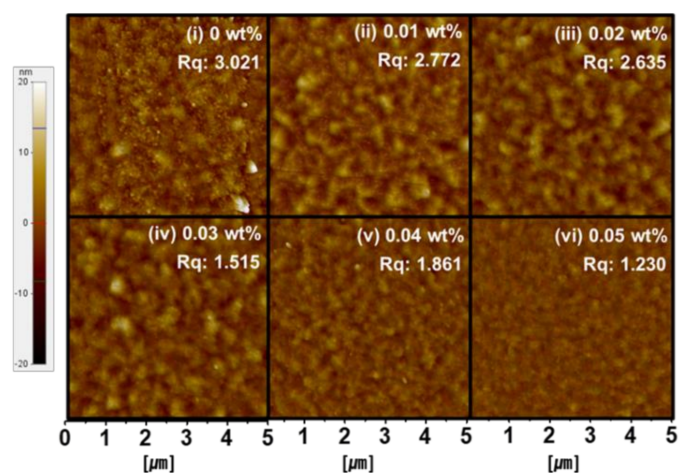
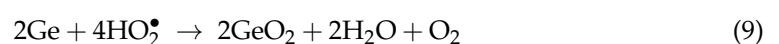
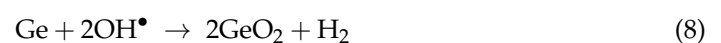
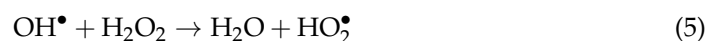
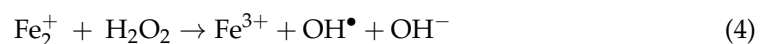
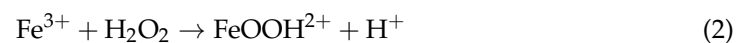
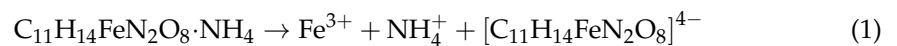


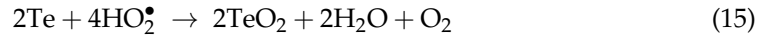
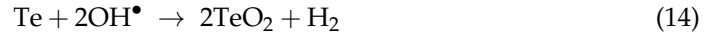
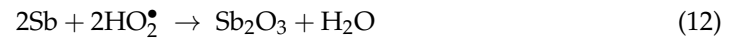
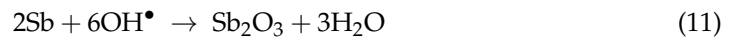
Figure 4. Dependency surface roughness of $\text{Ge}_1\text{Sb}_4\text{Te}_5$ film surface on ferric-ionic catalyst (i.e., PDTA-Fe) concentration after dipping of $\text{Ge}_1\text{Sb}_4\text{Te}_5$ film surface into slurries. The background AFM images estimated the presence of corrosion-induced pits and corrosion degree (i.e., Rq) on the $\text{Ge}_1\text{Sb}_4\text{Te}_5$ film surface after dipping.

3.2. Fenton Reaction Mechanism for Enhancing Polishing Rate and Suppressing Corrosion on the $\text{Ge}_1\text{Sb}_4\text{Te}_5$ Film Surface during CMP

The chemical passivation (i.e., oxidation) on the $\text{Ge}_1\text{Sb}_4\text{Te}_5$ film surface via the Fenton reaction was characterized by chemical composition analysis via XPS of the $\text{Ge}_1\text{Sb}_4\text{Te}_5$ film surface dipping into the slurries at 70 °C for 1 min. Without the Fenton reaction, the relative XPS peak intensities were at 1220-eV (i.e., GeO_2) and 1218-eV binding energy (i.e., Ge) were 40,232.6 and 23,321.9 a.u., as shown in Figure 5a. When the catalyst PDTA-Fe concentration increased from 0.01 to 0.05-wt%, the relative XPS peak intensity of GeO_2 increased exponentially from 54,128.1 and 158,677 a.u., while for Ge, it slightly decreased from 17,040.3 to 6467.8 a.u., as shown in the inset of Figure 5a. This result implies that the dissolved O_2 and radicals (i.e., HO_2^\bullet and OH^\bullet) via the Fenton reaction between the Fe^{3+} catalyst and H_2O_2 can oxidize the $\text{Ge}_1\text{Sb}_4\text{Te}_5$ film surface by producing GeO_2 , and the chemical oxidation degree of the $\text{Ge}_1\text{Sb}_4\text{Te}_5$ film surface linearly increased with the catalyst (i.e., PDTA-Fe) concentration. In addition, without the Fenton reaction, the relative XPS peak intensities at 539.5-eV binding energy (i.e., Sb_2O_3 of $\text{Sb}3d\ 3/2$) and 530-eV binding energy (i.e., Sb_2O_3 of $\text{Sb}3d\ 5/2$) were 108,718.2 and 307,888.6 a.u., as shown in Figure 5b. Both peaks linearly increased from 141,982 to 294,615.2 and 307,888.6 to 623,299.1 a.u., respectively, when the PDTA-Fe concentration increased from 0.01 to 0.05-wt%. Otherwise, the XPS peak intensities at 538-eV (i.e., Sb of $\text{Sb}3d\ 3/2$) and 528.2-eV (i.e., Sb of $\text{Sb}3d\ 5/2$) binding energy were independent of the catalyst PDTA-Fe concentration. This result also means that the Fenton reaction could oxidize easily the $\text{Ge}_1\text{Sb}_4\text{Te}_5$ film surface by producing a chemically oxidized layer (i.e., Sb_2O_3). Furthermore, without the Fenton reaction, the relative XPS peak intensities at 586-eV (i.e., TeO_2 of $\text{Te}3d\ 3/2$) and 576-eV (i.e., TeO_2 of $\text{Te}3d\ 5/2$) binding energies were 190430.6 and 274607 a.u., respectively, as shown in Figure 5c. Although, the catalyst PDTA-Fe concentration increased from 0.01 to 0.05-wt%, both peak intensities very slightly increased with the PDTA-Fe concentration. Moreover, the relative XPS peak intensities at 584-eV (i.e., Te of $\text{Te}3d\ 3/2$) and 573-eV (i.e., Te of $\text{Te}3d\ 5/2$) binding energies were almost independent of the catalyst PDTA-Fe concentration. This result indicates that the Ge and Sb atoms in the $\text{Ge}_1\text{Sb}_4\text{Te}_5$ film surface are well chemically oxidized rather than the Te atoms with dissolved O_2 and radicals (i.e., HO_2^\bullet and OH^\bullet). Thus, the formation of a chemically oxidized layer on the $\text{Ge}_1\text{Sb}_4\text{Te}_5$ film surface is mainly induced by Sb_2O_3 and TeO_2 rather than GeO_2 , and the chemical oxidation degree of Sb_2O_3 and TeO_2 was evidently enhanced with the catalyst PDTA-Fe concentration under the Fenton reaction. As a result, the polishing-rate of the $\text{Ge}_1\text{Sb}_4\text{Te}_5$ film surface linearly increased with the catalyst (i.e., PDTA-Fe) concentration, as shown in Figure 2.

The detailed Fenton reaction between the Fe^{3+} catalyst and H_2O_2 and chemical oxidation (i.e., formation of GeO_2 , Sb_2O_3 , and TeO_2) can be understood by the following equations [26–28].





First, PDTA-Fe (i.e., $\text{C}_{11}\text{H}_{14}\text{FeN}_2\text{O}_8 \cdot \text{NH}_4$) was dissolved with Fe^{3+} , NH_4^+ , and $[\text{C}_{11}\text{H}_{14}\text{N}_2\text{O}_8]^{4-}$ at pH 2, as shown in equation (1). The Fenton reaction between the Fe^{3+} catalyst and H_2O_2 generates dissolved O_2 and radicals (i.e., HO_2^\bullet , OH^\bullet , and $\text{O}^{\bullet-}_2$), as shown in Equations (2)–(7). As a result, chemically oxidized $\text{Ge}_1\text{Sb}_4\text{Te}_5$ film surface (i.e., formation of GeO_2 , Sb_2O_3 , and TeO_2) atoms are produced by the chemical reactions of Ge, Sb, and Te atoms with dissolved O_2 and radicals (i.e., HO_2^\bullet and OH^\bullet), as shown in Equations (8)–(16). The above equations indicate that the chemical oxidation degree of the $\text{Ge}_1\text{Sb}_4\text{Te}_5$ film surface increases linearly with the catalyst (i.e., PDTA-Fe) concentration.

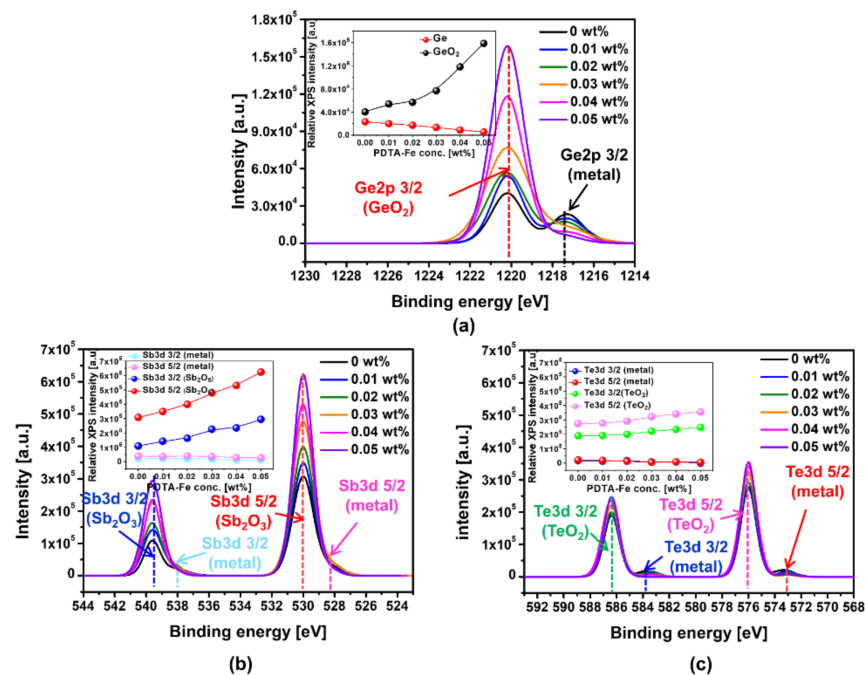


Figure 5. Dependency of chemical composition of $\text{Ge}_1\text{Sb}_4\text{Te}_5$ film surface on ferric-ionic catalyst (i.e., PDTA-Fe) concentration after dipping of $\text{Ge}_1\text{Sb}_4\text{Te}_5$ film surface into slurries. (a) Ge 2p spectra, (b) Sb 3d spectra, and (c) Te 3d spectra.

3.3. Effect of Corrosion Inhibitor with Protonated Amine Groups on Corrosion Suppression and Corrosion Inhibition Mechanism

Although the Fenton reaction in a $\text{Ge}_1\text{Sb}_4\text{Te}_5$ film surface CMP slurry can significantly suppresses CMP-induced corrosion on the $\text{Ge}_1\text{Sb}_4\text{Te}_5$ film surface, as shown in Figure 3, an actual $\text{Ge}_1\text{Sb}_4\text{Te}_5$ film surface CMP process using a Fenton reaction-based CMP slurry can also result in CMP-induced corrosion, producing a polishing-induced void or a recess at a nanoscale confined-structure PCRAM-cell [22,23]. Thus, to avoid corrosion at the nanoscale confined-structure PCRAM-cell after $\text{Ge}_1\text{Sb}_4\text{Te}_5$ film surface CMP, a corrosion inhibitor was mixed with the $\text{Ge}_1\text{Sb}_4\text{Te}_5$ film surface CMP slurry using the Fenton reaction. A corrosion inhibitor with a protonated amine functional group was selected, that is, polyethylenimine (PEI) with a molecular weight of 25,000 g/mol. The dependence of the potentiodynamic polarization curve for the corrosion potential (E_{corr}) vs. corrosion current density (I_{corr})

on the corrosion inhibitor (i.e., PEI) concentration was observed for the $\text{Ge}_1\text{Sb}_4\text{Te}_5$ film surface being dipped into the $\text{Ge}_1\text{Sb}_4\text{Te}_5$ film surface CMP slurry using the Fenton reaction and a corrosion inhibitor (i.e., PEI), as shown in Figure 6. From the potentiodynamic polarization curves in Figure 6a, the dependency of E_{corr} and I_{corr} on the corrosion inhibitor concentration was calculated, as shown in Figure 6b. When the corrosion inhibitor (i.e., PEI) concentration increased from 0 to 0.09 wt%, E_{corr} increased almost linearly from 0.28 to 0.3 V while I_{corr} decreased exponentially from -6.15 to -6.93 A/cm^2 . This result indicates that the addition of a corrosion inhibitor (i.e., PEI) into the $\text{Ge}_1\text{Sb}_4\text{Te}_5$ film surface CMP slurry clearly suppressed corrosion, and the corrosion inhibition degree was greatly enhanced with increasing PEI concentration.

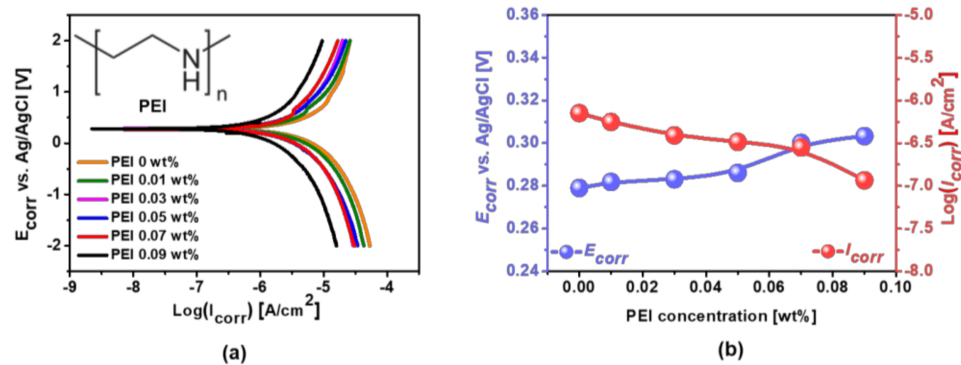


Figure 6. Dependency of corrosion degree of $\text{Ge}_1\text{Sb}_4\text{Te}_5$ film surface on corrosion inhibitor (i.e., PEI) concentration after dipping of $\text{Ge}_1\text{Sb}_4\text{Te}_5$ film surface into slurries. (a) Potentiodynamic polarization curve of $\text{Ge}_1\text{Sb}_4\text{Te}_5$ film surface as a function of corrosion inhibitor concentration. (b) Dependencies of corrosion potential (E_{corr}) vs. corrosion current density (I_{corr}) on corrosion inhibitor concentration.

To understand the mechanism by which PEI suppresses corrosion on the $\text{Ge}_1\text{Sb}_4\text{Te}_5$ film surface, the chemical composition of the $\text{Ge}_1\text{Sb}_4\text{Te}_5$ film surface after CMP using a Fenton reaction-based CMP slurry containing a corrosion inhibitor was analyzed by XPS as a function of the PEI concentration. NH_3^+ and NH_2^+ peak intensities adsorbed on the $\text{Ge}_1\text{Sb}_4\text{Te}_5$ film surface were found at 401.3 and 399.1 eV, respectively, as shown in Figure 7a. Note that both peaks represent the adsorption of a corrosion inhibitor (i.e., PEI) on the $\text{Ge}_1\text{Sb}_4\text{Te}_5$ film surface after CMP. Both peak intensities rapidly enhanced as soon as the PEI of 0.01-wt% was added in the $\text{Ge}_1\text{Sb}_4\text{Te}_5$ film surface CMP slurry and then very slightly increased with the PEI concentration when PEI concentration increased from 0.01 to 0.07-wt%, as shown in Figure 7b. With a further increase in the PEI concentration above 0.07-wt%, both peak intensities remarkably increased with increasing PEI concentration. In addition, the relative NH_3^+ peak intensity is approximately two times higher than the relative NH_2^+ peak intensity. The chemical composition analysis results evidently prove that a corrosion inhibitor (i.e., PEI) is well adsorbed on the $\text{Ge}_1\text{Sb}_4\text{Te}_5$ film surface, since the positively charged protonated amine groups (NH_3^+ and NH_2^+) of PEI are statically attractive to the negatively charged $\text{Ge}_1\text{Sb}_4\text{Te}_5$ film surface at pH 2. Note that the surface zeta potential of the $\text{Ge}_1\text{Sb}_4\text{Te}_5$ film surface at pH 2 is -1.29 mV, as shown in Figure S4. In addition, a higher concentration of the catalyst with protonated amine groups (i.e., NH_3^+ and NH_2^+) in a $\text{Ge}_1\text{Sb}_4\text{Te}_5$ film surface CMP slurry led to a higher adsorption of the catalyst on the $\text{Ge}_1\text{Sb}_4\text{Te}_5$ film surface. To observe how the adsorption of the catalyst affects the CMP performance, both $\text{Ge}_1\text{Sb}_4\text{Te}_5$ - and Si_3N_4 film polishing rates were estimated as a function of the corrosion inhibitor (i.e., PEI) concentration. The $\text{Ge}_1\text{Sb}_4\text{Te}_5$ film surface polishing rate slightly and linearly decreased from 90.2 to 67.2 nm/min when the corrosion inhibitor concentration increased from 0 to 0.09, as shown in Figure 8. In addition, the Si_3N_4 film surface polishing-rate decreased significantly from 4.8 to 0.97 nm/min when the corrosion inhibitor concentration increased from 0 to 0.03 and then saturated at ~ 0.9 nm/min for a further increase in the corrosion inhibitor concentration. The effect of the corrosion inhibitor

on the suppression of CMP-induced corrosion was clearly observed by observing the SEM image of the $\text{Ge}_1\text{Sb}_4\text{Te}_5$ film surface after a CMP without a corrosion inhibitor, the relative corrosion-induced surface roughness (i.e., R_q of pixel intensity in SEM images) of the $\text{Ge}_1\text{Sb}_4\text{Te}_5$ film surface after a CMP was 14.8, as shown in (i) of Figures 8 and S5. As soon as a corrosion inhibitor (i.e., PEI) was added into the CMP slurry, the relative corrosion-induced surface roughness rapidly decreased from 3.24 to 2.25 when the corrosion inhibitor concentration changed from 0.01 to 0.09-wt%, as shown in the SEM images of (ii)–(vi) in Figure 8. In addition, we confirmed the R_q of the polished $\text{Ge}_1\text{Sb}_4\text{Te}_5$ film surface was ~ 0.362 nm, which is a typical surface performance of CMP, as shown in Figure S6. These results indicate that the addition of a corrosion inhibitor (i.e., PEI) in the CMP slurry evidently suppresses the degree of corrosion-induced surface roughness.

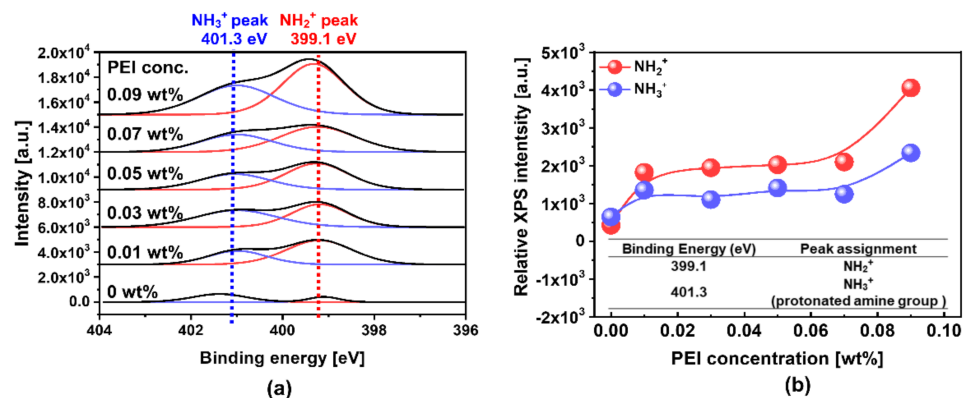


Figure 7. Dependency of chemical composition of $\text{Ge}_1\text{Sb}_4\text{Te}_5$ film surface on corrosion inhibitor (i.e., PEI) concentration after $\text{Ge}_1\text{Sb}_4\text{Te}_5$ film surface CMP. (a) NH_3^+ and NH_2^+ spectra. (b) Dependency of relative NH_3^+ and NH_2^+ peak intensity on corrosion inhibitor concentration of $\text{Ge}_1\text{Sb}_4\text{Te}_5$ film surface after CMP.

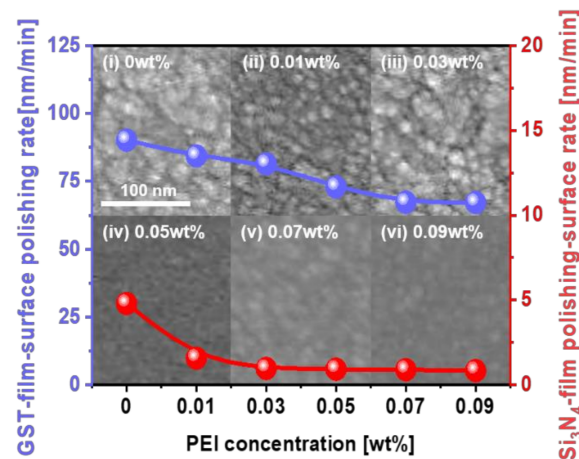


Figure 8. Dependency of $\text{Ge}_1\text{Sb}_4\text{Te}_5$ - and Si_3N_4 films polishing-rate on corrosion inhibitor (i.e., PEI) concentration. The background SEM images examined the presence of corrosion-induced pits on the $\text{Ge}_1\text{Sb}_4\text{Te}_5$ film surface after CMP.

In general, a PRAM cell is fabricated with a confined hole structure with a high aspect ratio (i.e., 4-nm in diameter and 60.7-nm height), as shown in Figure 9 [22,23]. The polishing rate of the $\text{Ge}_1\text{Sb}_4\text{Te}_5$ film surface without a confined-hole structure PRAM-cell array pattern in Figure 8 would be lower than that of the $\text{Ge}_1\text{Sb}_4\text{Te}_5$ film surface with a confined-hole structure PRAM-cell array pattern, because the polishing-rate of the $\text{Ge}_1\text{Sb}_4\text{Te}_5$ film surface in a confined-hole structure PRAM-cell array pattern could be enhanced because of the confined memory cell structure-induced stress [22,23]. Note

that a higher stress leads to a higher polishing rate. Thus, the dependence of the recess degree on the corrosion inhibitor concentration was observed by cross (x)-sectional TEM images of the confined PRAM cells after CMP. In this confined memory-cell structure, a CMP should be automatically stopped as soon as a stopping layer (i.e., Si_3N_4 layer) is exposed during CMP. Without using a corrosion inhibitor, the $\text{Ge}_1\text{Sb}_4\text{Te}_5$ layer in the confined-memory cell was completely etched off, owing to the severe corrosion of the $\text{Ge}_1\text{Sb}_4\text{Te}_5$ film surface, as shown in the empty confined-hole structure memory-cell (i.e., white image) in Figure 9a. As expected, the recess degree at the confined-hole structure memory-cells decreased significantly and linearly from 4.9 to 0.8 nm, when the corrosion inhibitor (i.e., PEI) concentration increased from 0.01 to 0.09 wt%, as shown in Figure 9b–f. This result indicates that the addition of a corrosion inhibitor (i.e., PEI) to a $\text{Ge}_1\text{Sb}_4\text{Te}_5$ film surface CMP slurry could evidently suppress the generation of corrosion-induced recess after a $\text{Ge}_1\text{Sb}_4\text{Te}_5$ film CMP; that is, a higher degree of suppression of corrosion via the corrosion inhibitor led to less recess on the surface of the confined-hole structure memory-cell after a CMP stopped on the stopping layer (i.e., Si_3N_4).

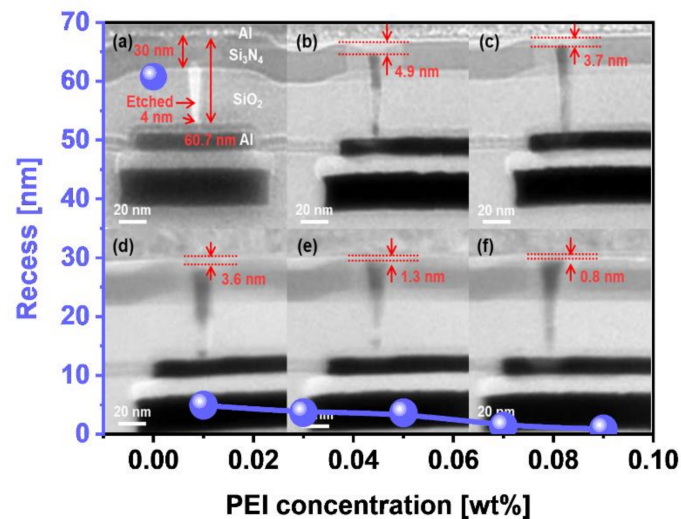


Figure 9. Dependency of polishing-induced recess on corrosion inhibitor (i.e., PEI) concentration. The background TEM images observed the presence of polishing-induced recess on the $\text{Ge}_1\text{Sb}_4\text{Te}_5$ film surface after CMP. PEI concentrations of (a) 0, (b) 0.01, (c) 0.03, (d) 0.05, (e) 0.07, and (f) 0.09 wt%.

4. Conclusions

To enhance the polishing rate of a $\text{Ge}_1\text{Sb}_4\text{Te}_5$ film surface and to minimize recess in a confined-hole structure PRAM-cell array pattern, the Fenton reaction was introduced, and a corrosion inhibitor (i.e., PEI) with protonated amine groups (i.e., NH_2^+ and NH_3^+) was added to a $\text{Ge}_1\text{Sb}_4\text{Te}_5$ film surface CMP slurry. The Fenton reaction between the ferric-ionic catalyst (i.e., PDTA–Fe) and H_2O_2 finally decomposed H_2O_2 into dissolved O_2 , OH^\bullet , and HO_2^\bullet in the slurry, as shown in Figure 10a. Then, the dissolved O_2 , OH^\bullet , HO_2^\bullet , and corrosion inhibitor (i.e., PEI) diffused and adsorbed on the $\text{Ge}_1\text{Sb}_4\text{Te}_5$ film surface as shown in Figure 10b. The adsorbed O_2 , OH^\bullet , and HO_2^\bullet on the $\text{Ge}_1\text{Sb}_4\text{Te}_5$ film surface chemically oxidized the $\text{Ge}_1\text{Sb}_4\text{Te}_5$ film surface by forming GeO_2 , Sb_2O_3 , and TeO_2 on the $\text{Ge}_1\text{Sb}_4\text{Te}_5$ film surface, as shown in Figure 10c. In particular, the higher sequence of chemical oxidation on the $\text{Ge}_1\text{Sb}_4\text{Te}_5$ film surface was followed by the forming of GeO_2 , Sb_2O_3 , and TeO_2 . As soon as the chemically oxidized layer composed of GeO_2 , Sb_2O_3 , and TeO_2 was produced on the $\text{Ge}_1\text{Sb}_4\text{Te}_5$ film surface, corrosion inhibitors with protonated amine groups (i.e., NH_2^+ and NH_3^+) were attached on the $\text{Ge}_1\text{Sb}_4\text{Te}_5$ film surface by the attractive force between protonated amine groups of corrosion inhibitors and the negatively charged chemically oxidized $\text{Ge}_1\text{Sb}_4\text{Te}_5$ film surface, thus causing a passivation of the organic layer of the film surface and suppressing corrosion, as shown in Figure 10c. Afterward, colloidal

silica abrasives polished off the chemically oxidized $\text{Ge}_1\text{Sb}_4\text{Te}_5$ film surface (having a passivated organic layer) via rubbing between the colloidal silica abrasives and the chemically oxidized $\text{Ge}_1\text{Sb}_4\text{Te}_5$ film surface; i.e., the CMP of the $\text{Ge}_1\text{Sb}_4\text{Te}_5$ film surface, as shown in Figure 10d. After several iterations of Figure 10a–d, the CMP automatically stopped as soon as the Si_3N_4 film surface was exposed, since corrosion inhibitors with protonated amine groups (i.e., NH_2^+ and NH_3^+) were preferentially attached to the highly negatively charged chemically oxidized Si_3N_4 film surface, as shown in Figure 10e. It should be noted that the polishing rate selectivity between the chemically oxidized $\text{Ge}_1\text{Sb}_4\text{Te}_5$ film surface and the Si_3N_4 film surface was 79:1, so that the patterned $\text{Ge}_1\text{Sb}_4\text{Te}_5$ film surface after CMP could attain a minimum recess (i.e., 0.8 nm). Therefore, the introduction of the Fenton reaction in a $\text{Ge}_1\text{Sb}_4\text{Te}_5$ film surface CMP slurry could significantly increase the polishing rate of the $\text{Ge}_1\text{Sb}_4\text{Te}_5$ film surface via efficient chemical oxidation (i.e., formation of GeO_2 , Sb_2O_3 , and TeO_2) on the $\text{Ge}_1\text{Sb}_4\text{Te}_5$ film surface. Moreover, the addition of corrosion inhibitors with protonated amine groups (i.e., NH_2^+ and NH_3^+) effectively coated the $\text{Ge}_1\text{Sb}_4\text{Te}_5$ film surface by forming an organic passivation layer on the $\text{Ge}_1\text{Sb}_4\text{Te}_5$ film surface to suppress corrosion. In particular, the protonated amine groups (i.e., NH_2^+ and NH_3^+) were preferentially highly negatively charged on the Si_3N_4 film surface rather than the negatively charged $\text{Ge}_1\text{Sb}_4\text{Te}_5$ film surface, so that the CMP was stopped and could achieve minimum recess of the $\text{Ge}_1\text{Sb}_4\text{Te}_5$ film surface. Because the Fenton reaction between the ferric–ionic catalyst and H_2O_2 is a strong exothermic reaction, after H_2O_2 was mixed with a CMP slurry, the remaining H_2O_2 decreased remarkably with time. Thus, research on the addition of a scavenger to suppress the Fenton reaction is essential for achieving stability of the CMP slurry.

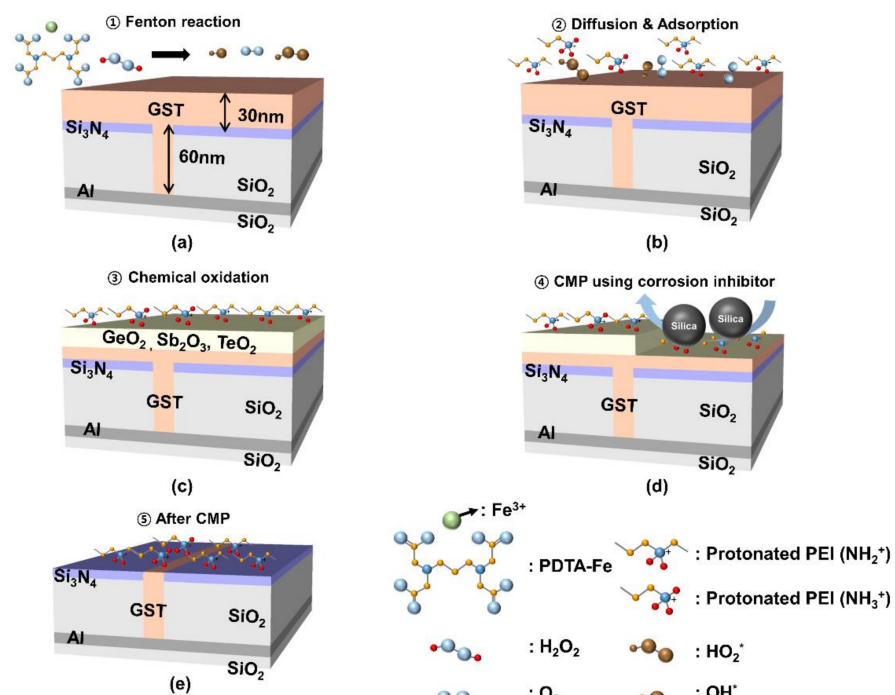


Figure 10. Schematic $\text{Ge}_1\text{Sb}_4\text{Te}_5$ film surface CMP mechanism using Fenton reaction and corrosion inhibitor. (a) Fenton reaction between ferric–ionic catalyst and H_2O_2 on as sputtered $\text{Ge}_1\text{Sb}_4\text{Te}_5$ film followed by laser annealing, (b) diffusion and adsorption of dissolved O_2 , OH^\bullet , HO_2^\bullet , and corrosion inhibitor (i.e., PEI) with protonated amine groups, (c) chemical oxidation via chemical reaction between $\text{Ge}_1\text{Sb}_4\text{Te}_5$ film surface, dissolved O_2 , OH^\bullet , and HO_2^\bullet , (d) mechanical rubbing between colloidal silica abrasives and chemically oxidized $\text{Ge}_1\text{Sb}_4\text{Te}_5$ film surface and passivation of corrosion inhibitor polymer, and (e) adsorption of corrosion inhibitor polymer on stopping layer (i.e., Si_3N_4 film) and $\text{Ge}_1\text{Sb}_4\text{Te}_5$ film surface after self-stopping of CMP.

Supplementary Materials: The following are available online at <https://www.mdpi.com/article/10.3390/app112210872/s1>, Figure S1: Material properties of Ge₁Sb₄Te₅ film subjected to sputtering followed by laser annealing, Figure S2: Pourbaix diagram for Ge₁Sb₄Te₅ film surface, Figure S3: Dependency of CMP performance on ferric ionic catalyst types and catalyst concentration for Fenton reaction of Ge₁Sb₄Te₅ film surface CMP slurry, Figure S4: Zeta potential of Ge₁Sb₄Te₅ film surface against pH, Figure S5: Dependency of relative surface roughness (i.e., pixel intensity) on the concentration of the corrosion inhibitor (i.e., PEI) determined using SEM images of the Ge₁Sb₄Te₅ film surface after CMP, Figure S6: Surface roughness (R_q) of the polished Ge₁Sb₄Te₅ film surface using Ge₁Sb₄Te₅ film surface CMP slurry including the PDTA-Fe of 0.05 wt% and PEI 0.09 wt%, measured by AFM in the scanning area 5 × 5 μm, Table S1: Chemical structure of ferric-ionic-catalysts.

Author Contributions: Conceptualization, G.-P.J. and J.-G.P.; methodology, G.-P.J.; investigation, Y.-H.S., P.-S.K., M.-H.H. and S.-W.H.; data curation, G.-P.J., J.-S.P.; writing—original draft preparation, G.-P.J.; writing—review and editing, J.-G.P.; validation, J.-H.P., H.C., B.-U.Y.; supervision, J.-G.P. All authors have read and agreed to the published version of the manuscript.

Funding: This research was funded by the MOTIE (Ministry of Trade, Industry and Energy), KSRC (Korea Semiconductor Research Consortium) and the Brain Korea 21 PLUS Program and Samsung Electronic Co., Ltd.

Institutional Review Board Statement: Not applicable.

Informed Consent Statement: Not applicable.

Data Availability Statement: Not applicable.

Acknowledgments: This research was supported by the MOTIE (Ministry of Trade, Industry and Energy (20010752)) and KSRC (Korea Semiconductor Research Consortium) support program for the development of future semiconductor devices and the Brain Korea 21 PLUS Program and the Samsung Electronic Co., Ltd. (IO200508-07328-01).

Conflicts of Interest: The authors declare no conflict of interest.

References

1. Makarov, A.; Sverdlov, V.; Selberherr, S. Emerging Memory Technologies: Trends, Challenges, and Modeling Methods. *Microelectron. Reliab.* **2012**, *52*, 628–634. [[CrossRef](#)]
2. Kim, M.K.; Kim, I.J.; Lee, J.S. CMOS-Compatible Ferroelectric NAND Flash Memory for High-Density, Low-Power, and High-Speed Three-Dimensional Memory. *Sci. Adv.* **2021**, *7*, 1–11. [[CrossRef](#)] [[PubMed](#)]
3. Kim, S.J.; Mohan, J.; Summerfelt, S.R.; Kim, J. Ferroelectric Hf_{0.5}Zr_{0.5}O₂ Thin Films: A Review of Recent Advances. *JOM* **2019**, *71*, 246–255. [[CrossRef](#)]
4. Raoux, S.; Burr, G.W.; Breitwisch, M.J.; Rettner, C.T.; Chen, Y.-C.; Shelby, R.M.; Salinga, M.; Krebs, D.; Chen, S.-H.; Lung, H.-L.; et al. Phase-Change Random Access Memory: A Scalable Technology. *IBM J. Res. Dev.* **2008**, *52*, 465–479. [[CrossRef](#)]
5. Yamada, N.; Ohno, E.; Nishiuchi, K.; Akahira, N.; Takao, M. Rapid-Phase Transitions of GeTe-Sb₂Te₃ Pseudobinary Amorphous Thin Films for an Optical Disk Memory. *J. Appl. Phys.* **1991**, *69*, 2849–2856. [[CrossRef](#)]
6. Wang, W.J.; Shi, L.P.; Zhao, R.; Lim, K.G.; Lee, H.K.; Chong, T.C.; Wu, Y.H. Fast Phase Transitions Induced by Picosecond Electrical Pulses on Phase Change Memory Cells. *Appl. Phys. Lett.* **2008**, *93*, 3–6. [[CrossRef](#)]
7. Lee, S.-Y.; Jeong, J.-H.; Cheong, B.-K. Overview of the Current Status of Technical Development for a Highly Scalable, High-Speed, Non-Volatile Phase-Change Memory. *J. Semicond. Technol. Sci.* **2008**, *8*, 1–10. [[CrossRef](#)]
8. Xiong, F.; Yalon, E.; Behnam, A.; Neumann, C.M.; Grosse, K.L.; Deshmukh, S.; Pop, E. Towards Ultimate Scaling Limits of Phase-Change Memory. In Proceedings of the 2016 IEEE International Electron Devices Meeting (IEDM), San Francisco, CA, USA, 3–7 December 2016; pp. 4.1.1–4.1.4. [[CrossRef](#)]
9. Kim, S.B.; Sosa, N.; Brightsky, M.; Mori, D.; Kim, W.; Zhu, Y.; Suu, K.; Lam, C. A Phase Change Memory Cell with Metal Nitride Liner as a Resistance Stabilizer to Reduce Read Current Noise for MLC Optimization. *IEEE Trans. Electron Devices* **2016**, *63*, 3922–3927. [[CrossRef](#)]
10. Cho, S.L.; Yi, J.H.; Ha, Y.H.; Kuh, B.J.; Lee, C.M.; Park, J.H.; Nam, S.D.; Horii, H.; Cho, B.O.; Ryoo, K.C.; et al. Highly Scalable On-Axis Confined Cell Structure for High Density PRAM beyond 256Mb. In Proceedings of the 2005 Symposium on VLSI Technology, Kyoto, Japan, 14–16 June 2005; Volume 2005, pp. 96–97. [[CrossRef](#)]
11. Feldmann, J.; Youngblood, N.; Li, X.; Wright, C.D.; Bhaskaran, H.; Pernice, W.H.P. Integrated 256 Cell Photonic Phase-Change Memory with 512-Bit Capacity. *IEEE J. Select. Top. Quantum Electron.* **2020**, *26*, 1–7. [[CrossRef](#)]
12. Fong, S.W.; Neumann, C.M.; Wong, H.-S.P. Phase-Change Memory—Towards a Storage-Class Memory. *IEEE Trans. Electron Devices* **2017**, *64*, 4374–4385. [[CrossRef](#)]

13. Tang, Q.; He, T.; Yu, K.; Cheng, Y.; Qi, R.; Huang, R.; Zhao, J.; Song, W.; Song, Z. The Effect of Thickness on Texture of Ge₂Sb₂Te₅ Phase-Change Films. *J. Mater. Sci. Mater. Electron.* **2020**, *31*, 5848–5853. [[CrossRef](#)]
14. Song, Z.; Wang, R.; Xue, Y.; Song, S. The “Gene” of Reversible Phase Transformation of Phase Change Materials: Octahedral Motif. *Nano Res.* **2021**, *12*–20. [[CrossRef](#)]
15. Zhang, Y.; Chen, Z.; Zhang, H. The Study of Deep Trench Etch Process for PCRAM. In Proceedings of the 2017 China Semiconductor Technology International Conference (CSTIC), Shanghai, China, 12–13 March 2017. [[CrossRef](#)]
16. Song, Y.J.; Ryoo, K.C.; Hwang, Y.N.; Jeong, C.W.; Lim, D.W.; Park, S.S.; Kim, J.I.; Kim, J.H.; Lee, S.Y.; Kong, J.H.; et al. Highly Reliable 256Mb PRAM with Advanced Ring Contact Technology and Novel Encapsulating Technology. In Proceedings of the 2006 Symposium on VLSI Technology, Honolulu, HI, USA, 13–15 June 2006; pp. 118–119. [[CrossRef](#)]
17. Kim, W.; Brightsky, M.; Masuda, T.; Sosa, N.; Kim, S.; Bruce, R.; Carta, F.; Fraczak, G.; Cheng, H.Y.; Ray, A.; et al. ALD-Based Confined PCM with a Metallic Liner Toward Unlimited Endurance. In Proceedings of the 2016 IEEE International Electron Devices Meeting (IEDM), San Francisco, CA, USA, 3–7 December 2016; pp. 4.2.1–4.2.4. [[CrossRef](#)]
18. Burr, G.W.; Shelby, R.M.; Sidler, S.; Di Nolfo, C.; Jang, J.; Boybat, I.; Shenoy, R.S.; Narayanan, P.; Virwani, K.; Giacometti, E.U.; et al. Experimental Demonstration and Tolerancing of a Large-Scale Neural Network (165 000 Synapses) Using Phase-Change Memory as the Synaptic Weight Element. *IEEE Trans. Electron Devices* **2015**, *62*, 3498–3507. [[CrossRef](#)]
19. Sebastian, A.; Le Gallo, M.; Burr, G.W.; Kim, S.; Brightsky, M.; Eleftheriou, E. Tutorial: Brain-Inspired Computing Using Phase-Change Memory Devices. *J. Appl. Phys.* **2018**, *124*, 111101. [[CrossRef](#)]
20. Sarwat, S.G. Materials Science and Engineering of Phase Change Random Access Memory. *Mater. Sci. Technol.* **2017**, *33*, 1890–1906. [[CrossRef](#)]
21. Kim, S.; Ishii, M.; Lewis, S.; Perri, T.; Brightsky, M.; Kim, W.; Jordan, R.; Burr, G.W.; Sosa, N.; Ray, A.; et al. NVM Neuromorphic Core with 64k-Cell (256-by-256) Phase Change Memory Synaptic Array with On-Chip Neuron Circuits for Continuous In-Situ Learning. In Proceedings of the 2015 IEEE International Electron Devices Meeting (IEDM), Washington, DC, USA, 7–9 December 2015; pp. 17.1.1–17.1.4. [[CrossRef](#)]
22. Kim, S.-B.; Cui, H.; Cho, J.-Y.; Seo, E.-B.; Yun, S.-S.; Son, Y.-H.; Jeong, G.-P.; Bae, J.-Y.; Park, J.-H.; Kang, S.-G.; et al. Surface-Tensile-Stress Induced Polishing-Voids Suppression via H₂O₂ Oxidizer Effect in Cross-Point Phase-Change-Memory-Cells. *ECS J. Solid State Sci. Technol.* **2019**, *8*, P667–P672. [[CrossRef](#)]
23. Kim, S.; Cui, H.; Cho, J.; Seo, E.; Yoon, S.; Son, Y.; Jeong, G.; Bae, J.; Park, J.; Park, J. Surface-Tensile-Stress Induced Polishing-Voids in Cross-Point Phase-Change-Memory Cells: Corrosion Mechanism and Solution. *Semicond. Sci. Technol.* **2019**, *34*, 65002. [[CrossRef](#)]
24. Feng, D.; Liu, W.; Liu, Y.; Song, Z.; Wang, W.; Wei, Z.; Zhao, G. Chemical Mechanical Planarization of Carbon-Doped Amorphous Ge₂Sb₂Te₅ Film with Hydrogen Peroxide as Oxidizer in Alkaline Slurry. *ECS J. Solid State Sci. Technol.* **2020**, *9*, 024007. [[CrossRef](#)]
25. Song, Z.; Liu, W.; Wang, L. Chemical mechanical polishing slurry for amorphous Ge₂Sb₂Te₅. *Procedia Eng.* **2015**, *102*, 582–589. [[CrossRef](#)]
26. Yun, S.S.; Son, Y.H.; Jeong, G.P.; Lee, J.H.; Jeong, J.H.; Bae, J.Y.; Kim, S.I.; Park, J.H.; Park, J.G. Dishing-Free Chemical Mechanical Planarization for Copper Films. *Colloids Surf. A Physicochem. Eng. Asp.* **2021**, *616*, 126143. [[CrossRef](#)]
27. Seo, E.-B.; Bae, J.-Y.; Kim, S.-I.; Choi, H.-E.; Son, Y.-H.; Yun, S.-S.; Park, J.-H.; Park, J.-G. Interfacial Chemical and Mechanical Reactions between Tungsten-Film and Nano-Scale Colloidal Zirconia Abrasives for Chemical-Mechanical-Planarization. *ECS J. Solid State Sci. Technol.* **2020**, *9*, 054001. [[CrossRef](#)]
28. Seo, E.-B.; Bae, J.-Y.; Kim, S.-I.; Choi, H.-E.; Kim, P.; Lee, J.-C.; Son, Y.-H.; Yun, S.-S.; Park, J.-H.; Park, J.-G. Influence of Scavenger on Abrasive Stability Enhancement and Chemical and Mechanical Properties for Tungsten-Film Chemical-Mechanical-Planarization. *ECS J. Solid State Sci. Technol.* **2020**, *9*, 065001. [[CrossRef](#)]